ELSEVIER

Journal of Materials Processing Technology 183 (2007) 77–87

Journal of Materials Processing Technology

www.elsevier.com/locate/jmatprotec

# Analytical modelling of residual stresses in machining

D. Ulutan, B. Erdem Alaca, I. Lazoglu *

*Department of Mechanical Engineering, Koc University, Rumeli Feneri Yolu, Sariyer, Istanbul 34450, Turkey*

Received 10 January 2006; received in revised form 25 September 2006; accepted 29 September 2006

**Abstract**

An analytical model is developed for prediction of residual stresses in machining. In the thermo-mechanical model of residual stresses both the thermal field of the workpiece and mechanical cutting forces are coupled. The shear energy created in the primary shear zone, the friction energy produced at the rake face–chip contact zone, the heat balance between the chip, tool and workpiece are considered based on the first law of thermodynamics. The temperature distributions on the workpiece, tool and chip are solved by using finite difference method. The calculated workpiece temperature field is used in thermal load calculations. Stresses resulting from thermal and mechanical loading are computed using an analytical elasto-plastic model and a relaxation procedure. The model is verified with experimental measurements of residual stresses on bearing steel 100Cr6 (JIS SUJ2) in the literature. With the analytical model presented here, substantial reduction in computational time is achieved in the predictions of residual stresses.
© 2006 Elsevier B.V. All rights reserved.

*Keywords:* Residual stress; Machining; Temperature; Force; Finite difference method; Plasticity

## 1. Introduction

It is well known that machining processes such as turning, milling and drilling, create undesirable tensile residual stresses on the surface of workpieces leading to a reduction in the fatigue life of parts. Residual stresses raise the need for over-tolerant specifications on the parts or require post-processing in order to remove tensile residual stresses. It is very critical to find a fast and precise solution to predict residual stresses in a machined component given the process parameters and material properties. Having a reliable simulation tool for residual stresses allows production engineers to select appropriate cutting conditions in advance. This facilitates the elimination of residual stresses or even altering the state of residual stresses to increase fatigue life using optimum machining conditions [1].

Different approaches to the determination of residual stresses can be summarized as experimental measurements, finite element calculations and analytical models. Although it serves as the ultimate validation tool for numerical or analytical simulations, experimental approach is too costly to be utilized in every scenario. On the other hand, finite element modelling serves as a good simulation tool; however, it is too time-consuming even with state of the art computational resources. And finally, analytical modelling provides a fast alternative. In the following, a comparison of these approaches is given.

Since the pioneering works in 1950s [2], a substantial amount of experimental work has accumulated regarding the development of residual stresses as a function of cutting parameters and the properties of the tool and the workpiece. The effects of feed rate, depth of cut, cutting speed, coolant, shape of the cutting edge, tool wear, tool coating, and workpiece hardness on residual stresses can be investigated separately, where residual stresses are measured after a carefully controlled machining process using a variety of techniques ranging from X-ray diffraction [3,4] to hole drilling [5,6] and deflection-etching [7]. Various materials including steel [3,5,8,9], ceramics [10,11] and composites [12] have been subjected to similar measurements. Some of the observed effects can be summarized as follows.

The decisive effect of workpiece hardness on residual stress distribution is observed to occur through the shear angle, where large shear angles lead to a tendency towards compressive residual stresses [13]. Liu and Barash [8] observed in their orthogonal cutting experiments on low-carbon steel that the length of the shear plane determines the depth over which residual stresses exist, while the shape of the cutting edge determines residual stress very near the machined surface. A similar conclusion regarding the dominant effect of tool nose radius on residual stresses at the surface was reached by Liu et al. [14] during

* Corresponding author. Tel.: +90 212 338 1587; fax: +90 212 338 1548.
*E-mail address:* ilazoglu@ku.edu.tr (I. Lazoglu).

0924-0136/$ – see front matter © 2006 Elsevier B.V. All rights reserved.
doi:10.1016/j.jmatprotec.2006.09.032

hard turning of bearing steel JIS SUJ2. The effect is observed to decrease with increasing tool wear. The influence of tool edge geometry was also confirmed by Thiele et al. [15] during hard turning on AISI 52100 steel and by Arunachalam et al. [16] on Inconel 718 alloy where increasing nose radius leads to tensile stresses. Increasing cutting speed, another major influence, is observed to result in tensile residual stresses in experiments using tungsten carbide tool on AISI 316L steel [3], WC tool on gamma TiAl [10] or cubic boron nitride tool on Inconel 718 alloy [17]. In the same work [17], an increase in the depth of cut is observed to lead to a reduction in compressive stresses at the entry and increase in tensile stresses at the exit, while there are reports describing the effect of the depth of cut on residual stresses as minimal [4]. The influence of feed rate is similarly reported to be minor [3,9]. The use of coolants, on the other hand, is observed to result in a shift in the compressive direction [17].

Modelling efforts, on the other hand, can be traced back to Merwin and Johnson's work [18] analyzing plastic deformation during repeated rolling contact on an elastic-perfectly plastic material under plane strain and predicting the variation of residual stresses with the distance from the contact surface. As an alternative, the stress invariant approach was developed by Jiang and Sehitoglu [19], where stresses during elastic–plastic rolling contact are taken to be equivalent to the elastic solution, which is then subjected to a relaxation procedure to meet the residual stress and strain conditions. Their results compared favorably well with finite element predictions and experimental measurements. However, most of the contact mechanics work does not take thermal loading into account. There are also phenomenological approaches to machining such as [7,20] where the deformation field beneath the surface is approximated by curve fitting of experimentally observed data. Nevertheless there is a lack of rigorous analytical treatment of the machining process with all of its aspects, including both mechanical and thermal loads.

Finally, since 1970s finite element analysis has been increasingly employed in machining problems. Saito et al. [21] and Akiyama et al. [22] used finite element analysis to predict thermal stresses during cutting. Iwata et al. [23] used a rigid-plastic model to analyze steady-state cutting with low cutting speed and low strain rates. As an improvement, Strenkowski and Carroll III [24] used an elasto-plastic model for the workpiece. Since these early works, different modelling approaches such as chip separation criterion or remeshing technique have been developed [25] and a variety of parametric studies for residual stress prediction is carried out. Ee et al. [25] developed an elastic–viscoplastic model and observed a significant influence of sequential cuts on residual stresses. An increase in the tool rake angle is observed to lead to an increase in tensile residual stresses in the cutting direction [26]. The effect of tool flank wear length is investigated by Lin et al. [27], and it is concluded that with increasing tool flank wear the compressive stresses increase. Lin et al. [28] also investigated the influences of depth of cut and cutting speed. Residual stress distributions in hard turning and grinding are compared by Guo and Barkey [29] using finite element analysis and their implications for fatigue are discussed. Hard turning is also investigated by Hua et al. [30,31], and according to their results, a high feed rate, high workpiece hardness or an increase in hone radius develop large compressive stresses. A three-dimensional finite element model developed by El-Wardany et al. [32] showed the significant effect of cutting temperature on residual stresses during hard turning. Another three-dimensional finite element study on a composite workpiece by El-Gallab and Sklad [33] concluded that although increase in feed rate leads to minor changes, an increase in cutting speed results in a major shift in stresses in tensile direction. Finite element method is also applied to residual stress predictions in processes other than turning or grinding such as electric discharge machining [34].

It is evident that in order to select appropriate cutting conditions, a fast and precise prediction of residual stresses is very much desired in various fields such as automotive and aerospace industries. Knowledge of material properties and machining conditions on the one hand, and thermo-mechanical analysis of the process on the other hand allow one to fulfill this desire with the analytical modelling technique presented in this paper. Compared to finite element approach, considerable reductions in simulation time can be achieved thanks to its analytical nature. Such a simulation tool not only lets the prediction of residual stresses to be achieved fast and precisely, which is a crucial factor from an engineering perspective, but also, from a scientific perspective, it allows one to understand the effects of each parameter on the system in detail and to optimize the process as well.

In this work, an analytical approach is adopted and a thermal model for the chip, tool and workpiece is presented first. The calculated temperature field is then utilized in a thermo-mechanical model along with cutting forces to calculate residual stresses due to thermal and mechanical loading. Thermo-mechanical model is concluded with verification of simulations by experimental data obtained on bearing steel 100Cr6 (JIS SUJ2) as reported in [14].

## 2. Thermal modelling of chip, tool and workpiece

In this section, machining is studied by modelling the heat transfer between tool, chip and workpiece. The shear energy created in the primary shear zone, the friction energy produced at the rake face–chip contact zone, the heat balance between the chip, tool and workpiece are considered. The temperature distribution is solved using finite difference method. Details of the temperature modelling can be found in [35]. Here, in this section, a short introduction is made for the thermal model used in the residual stress model.

### 2.1. The heat balance equations

Heat generation mechanisms in the primary shear zone and in the secondary friction zone, and heat balance equations based on the first law of thermodynamics for chip, tool and workpiece thermal fields are briefly written in the finite difference forms below.

### 2.2. Heat generated in the primary and secondary zones

In the temperature field predictions for the chip, tool and workpiece, which are based on the finite difference method uti-

lized for the machining operations. Heat generated per unit depth of cut in the primary and secondary zones are given as follows, respectively [35].

$$\dot{Q}_s = F_s V_s = \frac{\tau c V_w \cos(\alpha_n)}{\sin(\phi_n)\cos(\phi_n - \alpha_n)},$$
$$\dot{Q}_f = F_f V_c = \frac{\tau c V_w \sin(\beta_n)}{\cos(\phi_n + \beta_n - \alpha_n)\sin(\phi_n - \alpha_n)} \quad (1)$$

where $F_s$, $F_f$, $V_w$, $V_s$ and $V_c$ are the shear force in the shear plane, the frictional force between the tool rake face and the chip contact zone, the cutting velocity, the cutting velocity component along the shear plane and the cutting velocity component along the rake face, respectively. $\tau$, $\varphi_n$, $\alpha_n$ and $\beta_n$ are the shear flow stress in the shear plane, shear angle, normal rake angle and normal friction angle, respectively. $c$ is the instantaneous uncut chip thickness ($c$ = feed per revolution for turning).

The average temperature rise of the chip per unit depth of cut due to the shearing is determined by Oxley's energy partition function [36]:

$$\Delta\bar{T} = \frac{\dot{Q}_s(1-\chi)}{\rho c_c h V_w} \quad (2)$$

where $\rho$ and $c_c$ are the mass density and specific heat capacity of the chip, respectively. $\chi$ represents the proportion of the shearing flux entering into the workpiece, and is defined by

$$\chi = 0.5 - 0.35\log_{10}(R_t, \tan(\varphi_n)) \quad \text{for}$$
$$0.004 \le R_t\tan(\phi_n) \le 10,$$
$$\chi = 0.5 - 0.15\log_{10}(R_t, \tan(\varphi_n)) \quad \text{for} \quad R_t\tan(\phi_n) \ge 10 \quad (3)$$

where $R_t = cV_w/\zeta$ is the thermal number; $\zeta$ the thermal diffusivity defined as $k/(\rho c)$ in which $k$, $\rho$, $c$ represent conductivity, mass density and specific heat capacity of medium, respectively.

The average temperature rise on the shear plane is used as a boundary condition at point D in Fig. 1, and the heat generated in the primary and secondary zones are used as heat sources in solving the temperature distribution within the tool, chip and workpiece as presented in the following subsections.

### 2.3. Chip temperature model

The chip can be considered as a medium which is in quasi-static thermal equilibrium during an infinitesimal time. By considering orthogonal cutting (Fig. 1), with two-dimensional heat flow and one-dimensional mass transfer, the heat balance equation for the discrete chip zone can be written in the finite difference form in Cartesian coordinates as the following,

$$\frac{T_c(x+\delta x, y) + T_c(x-\delta x, y) - 2T_c(x,y)}{\delta x^2} + \frac{T_c(x, y+\delta y) + T_c(x, y-\delta y) - 2T_c(x,y)}{\delta y^2} + \dot{Q}_c(x,y) = \frac{\rho c_c}{k_c} V_c \frac{\delta T_c}{\delta x} \quad (4)$$

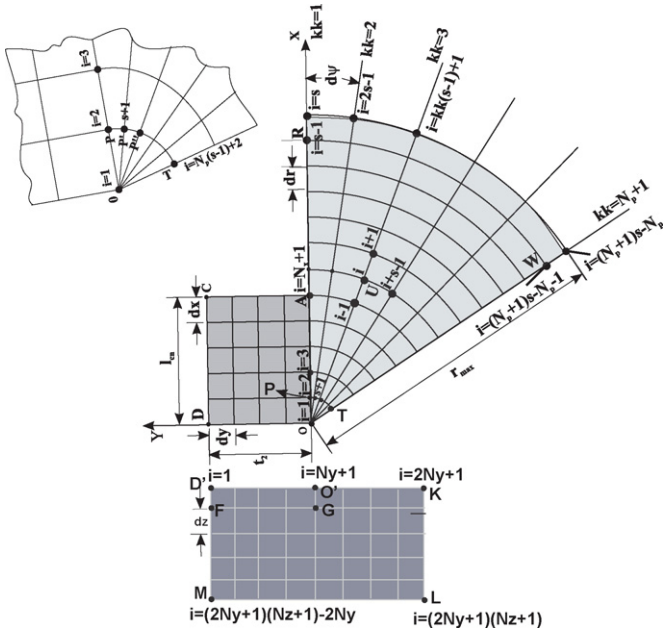


Fig. 1. Illustration of chip, tool and workpiece meshing.

where $\dot{Q}_c$, $k_c$, $c_c$ are also the energy generation rate per unit area in the differential chip zone, thermal conductivity and specific heat capacity of the chip, respectively.

The chip geometry must be meshed into small discrete elements for the finite difference solution of the chip temperature field and the equilibrium equation above needs to be written for each nodal point of the chip. The aspect ratio of the mesh can be unity to simplify the solutions, $\delta x = \delta y$.

In the equilibrium equation (Eq. (4)), the heat flow into the differential chip control zone ($\dot{Q}_c$) from the frictional heat source can be localized for each node along the chip–tool contact length as

$$\dot{Q}_{c(i)} = \frac{(1-B_i)\dot{Q}_f\,dx}{l_{cn}k_c} \quad \text{if and only if } 1 \le i \le N_x + 1 \quad (5)$$

where $B_i$ represents the proportion of the frictional heat flowing into the tool at the $i$th nodal point and it is unknown, initially. $\dot{Q}_f$, $l_{cn}$ and $N_x$ are the frictional heat generation rate, chip tool contact length and number of grids along the $x$-axis, respectively. It should be noticed that a uniform heat generation was considered along the chip–tool contact length. The internal nodes (all nodes other than $1 \le i \le N_x + 1$) will physically have no heat generation input. Therefore, $\dot{Q}_{c(i)}$ will be zero for all these nodes. Equilibrium equations for all of the nodes of the chip can be written as shown in Eq. (4), and all these equilibrium equations can be collected in a compact matrix form, and, therefore, the temperature of each nodal point in the chip nodal network corresponds to a value in the chip temperature array $\{T_c\}$ can be determined as

$$[A]\{T_c\} = \{C\} \rightarrow \{T_c\} = [A]^{-1}\{C\} \quad (6)$$

where $[A]$ is the square coefficient matrix determined from Eq. (4); $\{T_c\}$ the chip temperature array; $\{C\}$ is the heat generation array. Writing the equilibrium equation for each nodal point

leads to the following elements of coefficient matrix [$A$], and heat generation array $\{C\}$.

### 2.4. Tool temperature model

Whereas Cartesian coordinates are used for the chip, applying polar coordinates to the tool is advantageous due to the mathematical accuracy and its convenience in the computational implementation of the model. The heat transfer equilibrium equations for the control zone around the tool nodal points can be written in the finite difference form in polar coordinates as the following:

$$\frac{T_{t(r+\delta r,\psi)} + T_{t(r-\delta r,\psi)} - 2T_{t(r,\psi)}}{\delta r^2} + \frac{T_{t(r+\delta r,\psi)} - T_{t(r-\delta r,\psi)}}{2r\delta r} + \frac{T_{t(r,\psi+\delta\psi)} + T_{t(r,\psi-\delta\psi)} - 2T_{t(r,\psi)}}{r^2\delta\psi^2} + \dot{Q}_t = 0 \quad (7)$$

where $T_t$ represents the tool temperature field; $r$ the radial distance between the nodal point in concern and the tool tip shown as point O in Fig. 1; $\psi$ is the angular position of the nodal point. $k_t$ and $\dot{Q}_t$ denote the tool thermal conductivity and heat generation rate per unit area in the control zone, respectively.

The frictional heat flow rate into the tool is given by

$$\dot{Q}_{t(i)} = \frac{B_i \dot{Q}_f \delta x}{l_{cn} k_t}, \quad \text{if and only if } 1 \le i \le N_x + 1 \quad (8)$$

Similar to the chip heat balance equations, the equilibrium equations for all nodal points of the tool can be written and collected in a compact form, and, therefore, the tool temperature distribution can be determined from

$$[D]\{T_t\} = \{E\} \rightarrow \{T_t\} = [D]^{-1}\{E\} \quad (9)$$

where [$D$] is the square coefficient matrix determined from Eq. (7); $\{T_t\}$ the tool temperature array; $\{E\}$ is the heat generation array for the tool.

If the same procedure defined in Cartesian coordinates is followed and the finite difference equilibrium equation of the tool (Eq. (7)) is written for each nodal point of the tool in polar coordinates, to the following elements of coefficient matrix [$D$], and heat generation array $\{E\}$ is obtained.

In the above equations besides the tool and chip temperature distribution, the partitions of the heat ($B_i$) at the nodal points along the chip workpiece contact length are not known initially. Therefore, a recursive process is required for the computation. Initial values between 0 and 1 can be assigned for the heat partition at each nodal point. The tool and chip temperature fields can be determined based on the initial assignment of $B_i$. After solving the chip and tool heat balance equations (Eqs. (6) and (9)), if temperatures of the corresponding tool and chip nodal points, at which tool and chip are in contact, are different than each other, then the heat partition value for the corresponding nodal points needs to be modified. Thus, at the end of the recursive solution, the temperature fields of the tool and chip can be determined from $\{T_t\}$, $\{T_c\}$.

### 2.5. Workpiece temperature model

Considering the geometry of the system, a first order approximation can be performed and the workpiece can be assumed as a rectangular body. Therefore; Cartesian coordinates can be applied to the workpiece. Similar to chip heat balance equations, the equilibrium equations for all nodal points of the workpiece can be written and collected in a compact form. Workpiece temperature distribution can be determined from,

$$[R]\{T_w\} = [S] \rightarrow \{T_w\} - [R]^{-1}[S] \quad (10)$$

where $R$ is the square coefficient matrix; $\{T_w\}$ the workpiece temperature array; $\{S\}$ is the heat generation array for the workpiece. The heat conducted into the work material can be found by using Oxley's energy partition function [36], which is explained in Eq. (3).

## 3. Thermo-mechanical modelling of stresses

### 3.1. Elastic loading

Fig. 2 shows the geometry of the problem. The cutting force is modeled as a distributed load with radial and tangential tractions of magnitude $f_r$ and $f_t$, respectively. These tractions are defined in the oblique coordinate system corresponding to the actual cutting geometry and transformed to the orthogonal coordinate system of Fig. 2 enabling one to reduce the problem to two dimensions. The workpiece is modeled as a semi-infinite, homogeneous, isotropic, elasto-plastic material exhibiting rate-independent, isotropic hardening with a von Mises yield surface. The elastic modulus and the Poisson's ratio of the workpiece are denoted as $E$ and $\upsilon$, respectively. Coefficient of thermal expansion is $\alpha$ and the plastic modulus is given as $h$. The temperature distribution within the workpiece during the cutting process is calculated using finite difference method as briefly explained in the previous section. The following section is dedicated to calculating stresses within the material due to both mechanical and thermal loading.

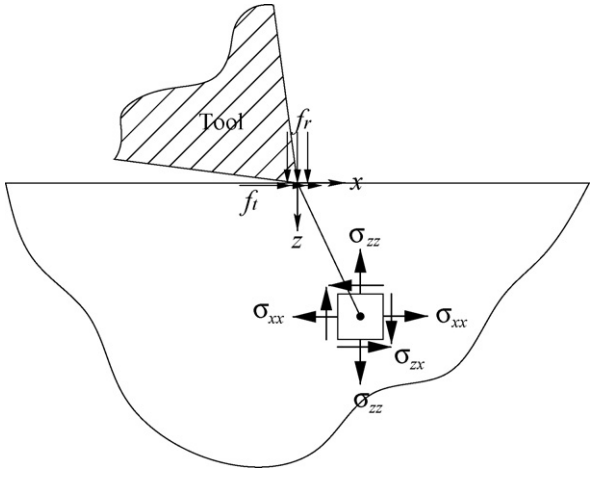


Fig. 2. The geometry of the plane strain problem. Stresses resulting from mechanical and thermal loading are expressed in terms of the coordinate system shown here with the $y$-axis pointing out of the plane of the drawing.

Let us first consider mechanical loading due to cutting forces. Assuming a state of plane strain in $y$ direction ($\varepsilon_{yy}=0$), stresses under the normal compressive pressure, $f_r$, and tangential traction, $f_t$, as given with the associated coordinate system in Fig. 2, are calculated using the following equations [37]:

$$\sigma_{xx}^{\text{mech}} = -\frac{2z}{\pi}\int_{-a}^{a}\frac{f_r(x-s)^2\,\mathrm{d}s}{((x-s)^2+z^2)^2} - \frac{2}{\pi}\int_{-a}^{a}\frac{f_t(x-s)^3\,\mathrm{d}s}{((x-s)^2+z^2)^2},$$

$$\sigma_{zz}^{\text{mech}} = -\frac{2z^3}{\pi}\int_{-a}^{a}\frac{f_r\,\mathrm{d}s}{((x-s)^2+z^2)^2} - \frac{2z^2}{\pi}\int_{-a}^{a}\frac{f_t(x-s)\,\mathrm{d}s}{((x-s)^2+z^2)^2},$$

$$\sigma_{xz}^{\text{mech}} = -\frac{2z^2}{\pi}\int_{-a}^{a}\frac{f_r(x-s)\,\mathrm{d}s}{((x-s)^2+z^2)^2} - \frac{2z}{\pi}\int_{-a}^{a}\frac{f_t(x-s)^2\,\mathrm{d}s}{((x-s)^2+z^2)^2} \tag{11}$$

where the span of the integrals $[-a, a]$, is a function of the cutting edge radius.

On the other hand, thermal stresses due to non-uniform temperature distribution, $T$, within the workpiece are calculated by superposing,

(i) stresses due to body forces $X=-(\alpha E/(1-2\nu))(\delta T/\delta x)$ and $Z=-(\alpha E/(1-2\nu))(\delta T/\delta z)$,
(ii) stresses due to a tensile surface traction of $\alpha ET/(1-2\nu)$,
(iii) a hydrostatic pressure of $\alpha ET/(1-2\nu)$ [38].

The resulting thermal stress components are given as [37,39]

$$\sigma_{xx}^{\text{therm}} = -\frac{\alpha E}{1-2\nu}\int_0^{\infty}\int_{-\infty}^{\infty}\left(G_{x\text{h}}\frac{\partial T}{\partial x}(x',z')+G_{x\text{v}}\frac{\partial T}{\partial z}(x',z')\right)\times \mathrm{d}x'\,\mathrm{d}z' + \frac{2z}{\pi}\int_{-\infty}^{\infty}\frac{p(t)(t-x)^2}{((t-x)^2+z^2)^2}\,\mathrm{d}t - \frac{\alpha ET(x,z)}{1-2\nu},$$

$$\sigma_{zz}^{\text{therm}} = -\frac{\alpha E}{1-2\nu}\int_0^{\infty}\int_{-\infty}^{\infty}\left(G_{z\text{h}}\frac{\partial T}{\partial x}(x',z')+G_{z\text{v}}\frac{\partial T}{\partial z}(x',z')\right)\times \mathrm{d}x'\,\mathrm{d}z' + \frac{2z^3}{\pi}\int_{-\infty}^{\infty}\frac{p(t)}{((t-x)^2+z^2)^2}\,\mathrm{d}t - \frac{\alpha ET(x,z)}{1-2\nu},$$

$$\sigma_{xz}^{\text{therm}} = -\frac{\alpha E}{1-2\nu}\int_0^{\infty}\int_{-\infty}^{\infty}\times\left(G_{xz\text{h}}\frac{\partial T}{\partial x}(x',z')+G_{xz\text{v}}\frac{\partial T}{\partial z}(x',z')\right)\mathrm{d}x'\,\mathrm{d}z' + \frac{2z^2}{\pi}\int_{-\infty}^{\infty}\frac{p(t)(x-t)}{((t-x)^2+z^2)^2}\,\mathrm{d}t \tag{12}$$

where

$$p(t) = \frac{\alpha ET(x,z=0)}{1-2\nu}$$

and $G_{x\text{h}}$, $G_{x\text{v}}$, $G_{z\text{h}}$, $G_{z\text{v}}$, $G_{xz\text{h}}$, and $G_{xz\text{v}}$ are the plane strain Green's functions. For example, $G_{x\text{h}}(x, z, x', z')$ is the normal stress $\sigma_{xx}(x, z)$ due to a unit point body load at $(x', z')$ acting along the $x$ direction. Similarly, $G_{x\text{v}}(x, z, x', z')$ is the normal stress $\sigma_{xx}(x, z)$ due to a unit point body load at $(x', z')$ acting along the $z$ direction. These functions are used throughout this work as given by Saif et al. [39].

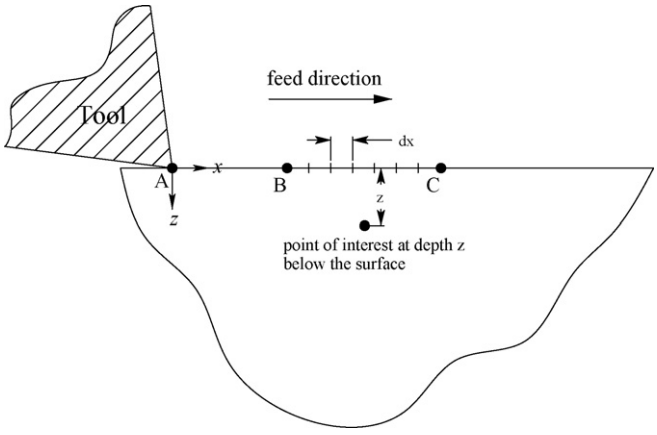


Fig. 3. The discretization of tool motion within the plastic zone BC.

Finally, mechanical and thermal stresses are added to compute the total elastic stress, *i.e.*

$$\sigma_{xx}^{\text{el}} = \sigma_{xx}^{\text{mech}} + \sigma_{xx}^{\text{therm}}, \qquad \sigma_{zz}^{\text{el}} = \sigma_{zz}^{\text{mech}} + \sigma_{zz}^{\text{therm}},$$
$$\sigma_{xz}^{\text{el}} = \sigma_{xz}^{\text{mech}} + \sigma_{xz}^{\text{therm}}, \qquad \sigma_{yy}^{\text{el}} = \nu(\sigma_{xx}^{\text{el}} + \sigma_{zz}^{\text{el}}) - \alpha ET \tag{13}$$

### 3.2. Loading beyond yielding

If the tip is far away (point A in Fig. 3), stresses are elastic at the point of interest, and hence, the formulation of the preceding section applies. The cutting tool tip travels in the positive $x$ direction carrying the origin of the coordinate system with itself. During this translation, stresses build up at the point of interest, and finally, say at point B in Fig. 3, plastic deformation starts and continues until the onset of elastic unloading at point C. In this section, the analytical approach utilized within this plastic zone will be considered.

Realizing the similarities between the loading and the resulting stress state of this problem and that of the elastic–plastic rolling contact case, we adopt the stress invariant assumption and subsequent relaxation procedure utilized in contact problems [19]. This assumption can be stated as

$$\sigma_{ij} = \sigma_{ij}^{\text{el}} \tag{14}$$

where $\sigma_{ij}$ stand for stress components. Specifically, for the case of plane strain explained in Fig. 2, Eq. (14) can be restated as

$$\sigma_{xx} = \sigma_{xx}^{\text{el}}, \qquad \sigma_{zz} = \sigma_{zz}^{\text{el}}, \qquad \sigma_{xz} = \sigma_{xz}^{\text{el}} \tag{15}$$

with the exception of $\sigma_{yy}$. In the following, the evolution of $\sigma_{yy}$ in the plastic regime is studied.

Assuming that the workpiece is isotropic and obeys the von Mises criterion for yielding, *i.e.* the yield surface is defined by

$$f = \frac{1}{2}S_{ij}S_{ij} - k^2 = 0 \tag{16}$$

where

$$S_{ij} = \sigma_{ij} - \frac{1}{3}\sigma_{kk}\delta_{ij} \quad \text{(deviatoric stresses)}$$

and $k$ is the current yield strength in pure shear, the "associated flow rule" or the so-called "normality" condition can be used to calculate plastic strain increments, $d\varepsilon_{ij}^{p}$:

$$d\varepsilon_{ij}^{p} = \frac{1}{2hk^2} S_{ij} S_{kl}\, d\sigma_{kl} \tag{17}$$

with $h$ as the plastic modulus is an indication of the change of the yield surface size as a function of plastic strain. In this approach, a rate-independent, purely isotropic hardening is assumed with the yield surface expanding or contracting uniformly without translation and without changing in shape. As a result, the Bauschinger effect is neglected. However, anisotropy upon unloading can easily be incorporated into the model by switching to kinematic hardening by taking into account the evolution of deviatoric back stresses as a new state variable [40]. For the sake of simplicity, Eq. (17) will be used throughout this paper.

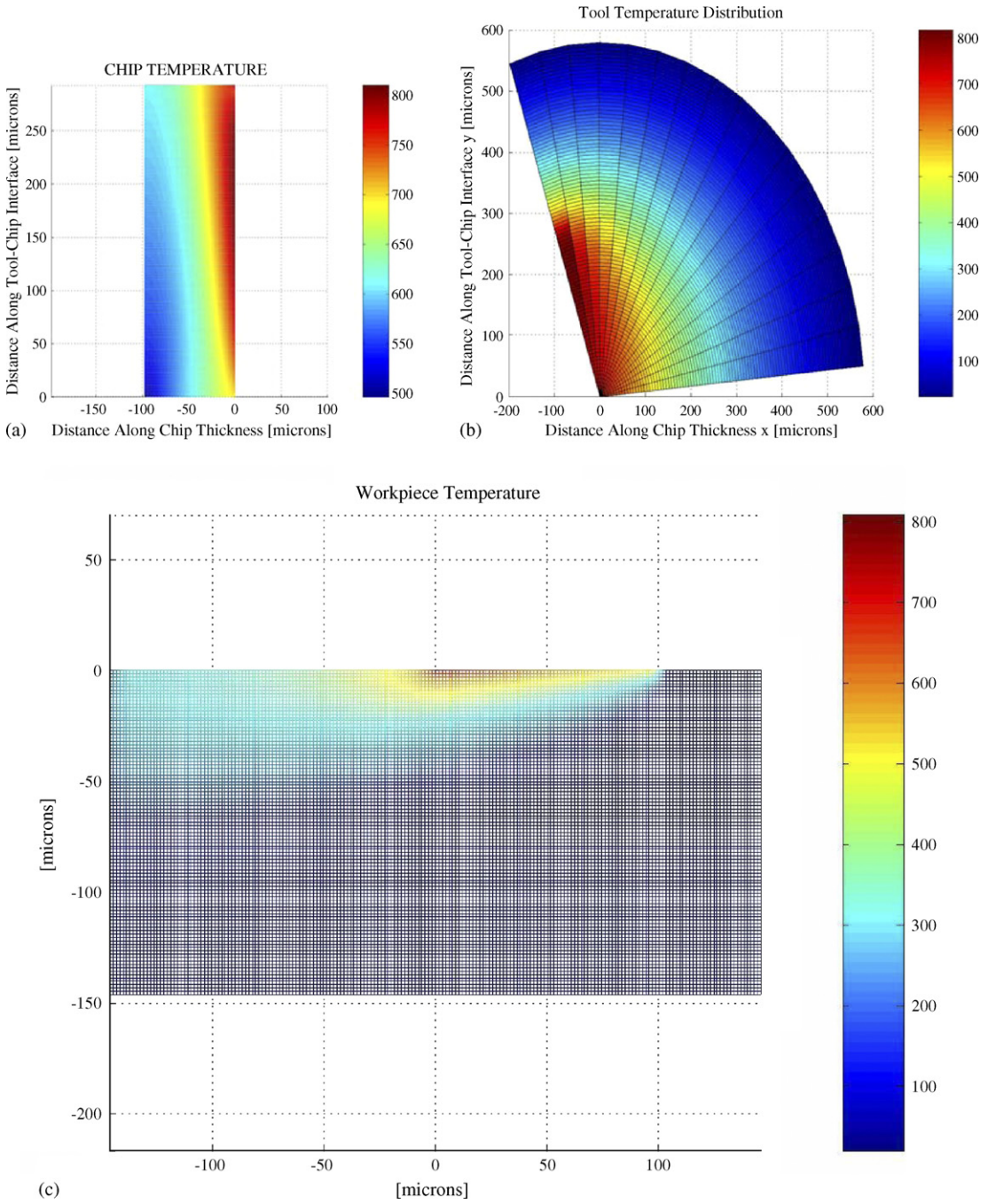


Fig. 4. Temperature field simulations for: (a) chip; (b) tool; (c) workpiece for a depth of cut of 0.1 mm.

Coming back to Fig. 3, stress increments $d\sigma_{xx}$, $d\sigma_{zz}$, and $d\sigma_{xz}$ are calculated according to Eq. (15), when the cutting tool is moved by an amount of $dx$ accompanied by a temperature change of $dT$. On the other hand, the increment $d\sigma_{yy}$ is calculated using stress components from the previous step and the fact that $d\varepsilon_{yy} = d\varepsilon_{yy}^{el} + d\varepsilon_{yy}^{therm} + d\varepsilon_{yy}^{p} = 0$. Since we know the elastic, thermal and plastic contributions to $d\varepsilon_{yy}$ with

$$d\varepsilon_{yy}^{el} = \frac{d\sigma_{yy}}{E} - \frac{\nu}{E}(d\sigma_{xx} + d\sigma_{zz}), \qquad d\varepsilon_{yy}^{therm} = \alpha\, dT,$$
$$d\varepsilon_{yy}^{p} = \frac{1}{2hk^2}(S_{xx}S_{yy}\, d\sigma_{xx} + S_{yy}S_{yy}\, d\sigma_{yy} + S_{zz}S_{yy}\, d\sigma_{zz} + 2S_{xz}S_{yy}\, d\sigma_{xz}) \tag{18}$$

corresponding $d\sigma_{yy}$ can be calculated in closed form as

$$d\sigma_{yy} = \frac{1}{1+\frac{E}{2hk^2}}\left\{\left(\nu - \frac{E}{2hk^2}S_{xx}S_{yy}\right)d\sigma_{xx} + \left(\nu - \frac{E}{2hk^2}S_{zz}S_{yy}\right)d\sigma_{zz} - \frac{E}{hk^2}S_{xz}S_{yy}\, d\sigma_{xz} - \alpha E\, dT\right\} \tag{19}$$

This procedure is repeated for every increment $dx$ until stresses start decreasing at the point of interest when the cutting tool moves away. Beyond this point (point C in Fig. 3), elastic unloading takes place where the full scope of Eq. (13) is again used. Once the elastic unloading is complete, *i.e.* the cutting forces no

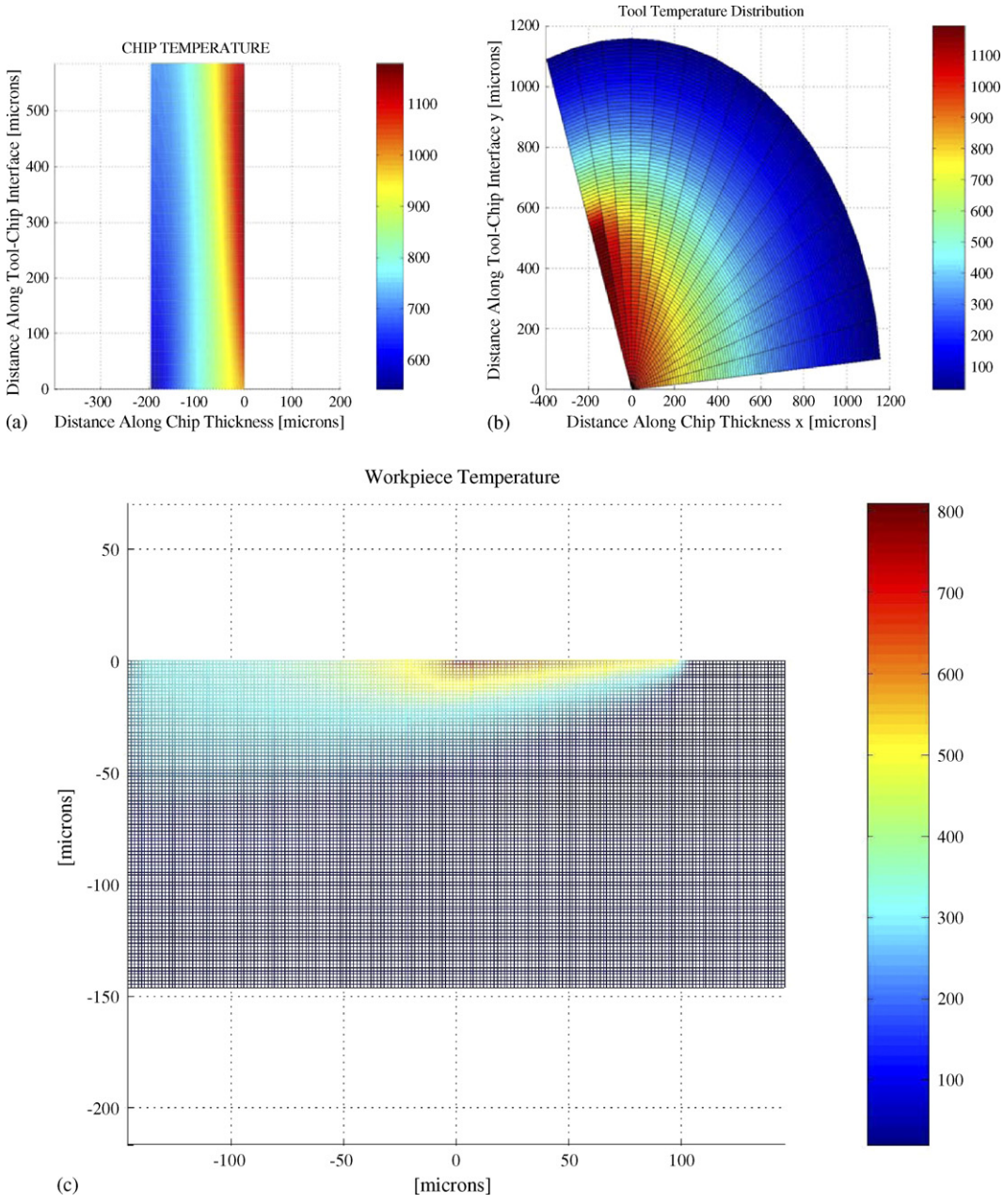


Fig. 5. Temperature field simulations for: (a) chip; (b) tool; (c) workpiece for a depth of cut of 0.2 mm.

longer produce any stresses at the point of interest and the temperature has decreased to its ambient value so that $T(x, z) = 0$, distributions of stresses and strains are determined. Next section deals with the final question of relating these stresses to the residual stresses through a relaxation procedure.

### 3.3. Final relaxation procedure

Before proceeding to the calculation of the magnitude of residual stresses, let us first consider the characteristics of individual components, $\sigma^{r}_{ij}$. The following discussion is mainly due to Merwin and Johnson [18].

Plane strain assumption along the $y$ direction leads to $\sigma^{r}_{xy} = \sigma^{r}_{zy} = \varepsilon^{r}_{yy} = \varepsilon^{r}_{xy} = \varepsilon^{r}_{zy} = 0$. The remaining stress and strain components should be also independent of $y$. Furthermore, if the plastic deformation takes place in a continuous manner, it can be assumed that the surface remains planar after deformation eliminating $\varepsilon^{r}_{xx}$ and making all other remaining stress and strain components independent of $x$. In order to retain equilibrium and a traction-free surface, $\sigma^{r}_{zz}$ and $\sigma^{r}_{xz}$ cannot exist. Hence, the expected outcome of the cutting process can be summarized as follows:

$$\sigma^{r}_{xx} = f_1(z), \quad \sigma^{r}_{yy} = f_2(z), \quad \sigma^{r}_{zz} = \sigma^{r}_{xz} = \sigma^{r}_{xy} = \sigma^{r}_{zy} = 0,$$
$$\varepsilon^{r}_{zz} = f_3(z), \quad \varepsilon^{r}_{xz} = f_4(z) \tag{20}$$

$$\varepsilon^{r}_{xx} = \varepsilon^{r}_{yy} = \varepsilon^{r}_{xy} = \varepsilon^{r}_{zy} = 0 \tag{21}$$

where $f_k(z)$ is a function of $z$, *i.e.* the depth of the point of interest.

However, when Eq. (14) is invoked, most of the resulting stresses and strains are non-zero, and hence, they do not satisfy Eqs. (20) and (21). Let us denote these non-zero components as $\varepsilon^{f}_{xx}$, $\sigma^{f}_{zz}$ and $\sigma^{f}_{xz}$. Therefore, stress and strain increments of Eq. (22) are enforced as a part of a relaxation procedure as proposed in [19].

$$d\varepsilon_{xx} = \frac{\varepsilon^{f}_{xx}}{M}, \quad d\sigma_{zz} = \frac{\sigma^{f}_{zz}}{M}, \quad d\sigma_{xz} = \frac{\sigma^{f}_{xz}}{M} \tag{22}$$

After a total of $M$ steps, stress and strain components in Eq. (22) are reduced to zero. Meanwhile, the corresponding changes in $\sigma_{xx}$ and $\sigma_{yy}$ are computed. If the relaxation is elastic, Hooke's Law is utilized in determining these two stresses. If yielding occurs, then Eqs. (23) and (24) are solved simultaneously to determine $d\sigma_{xx}$ and $d\sigma_{yy}$. Once the relaxation procedure is completed, the resulting $\sigma_{xx}$ and $\sigma_{yy}$ are taken as the residual stresses $\sigma^{r}_{xx}$ and $\sigma^{r}_{yy}$ along the feed direction and perpendicular to the feed direction, respectively.

$$\left\{\frac{E}{2hk^2}S_{xx}S_{yy} - \nu\right\} d\sigma_{xx} + \left\{\frac{E}{2hk^2}S_{yy}S_{yy} + 1\right\} d\sigma_{yy} + \left\{\frac{E}{2hk^2}S_{zz}S_{yy} - \nu\right\} d\sigma_{zz} + \left\{\frac{E}{hk^2}S_{xz}S_{yy}\right\} d\sigma_{xz} = 0 \tag{23}$$

$$\left\{\frac{E}{2hk^2}S_{xx}S_{xx} + 1\right\} d\sigma_{xx} + \left\{\frac{E}{2hk^2}S_{yy}S_{xx} - \nu\right\} d\sigma_{yy} + \left\{\frac{E}{2hk^2}S_{zz}S_{xx} - \nu\right\} d\sigma_{zz} + \left\{\frac{E}{hk^2}S_{xz}S_{xx}\right\} d\sigma_{xz} = d\varepsilon_{xx} \tag{24}$$

## 4. Simulations and validations

In order to validate the theoretical residual stress model, simulations were performed at experimental conditions reported by Liu et al. [14] on hard turning of bearing steel 100Cr6 (JIS SUJ2). In these tests CBN tools (Mitsubishi Materials, Grade MB825) with chamfer angle of 25°, cutting edge radius of 0.01 mm and nose radii of 0.4, 0.8 and 1.2 mm were used in dry cutting conditions. The cutting speed was 120 mm/min, feedrate was 0.1 mm/rev, and depth of cut was chosen to be 0.1 and 0.2 mm.

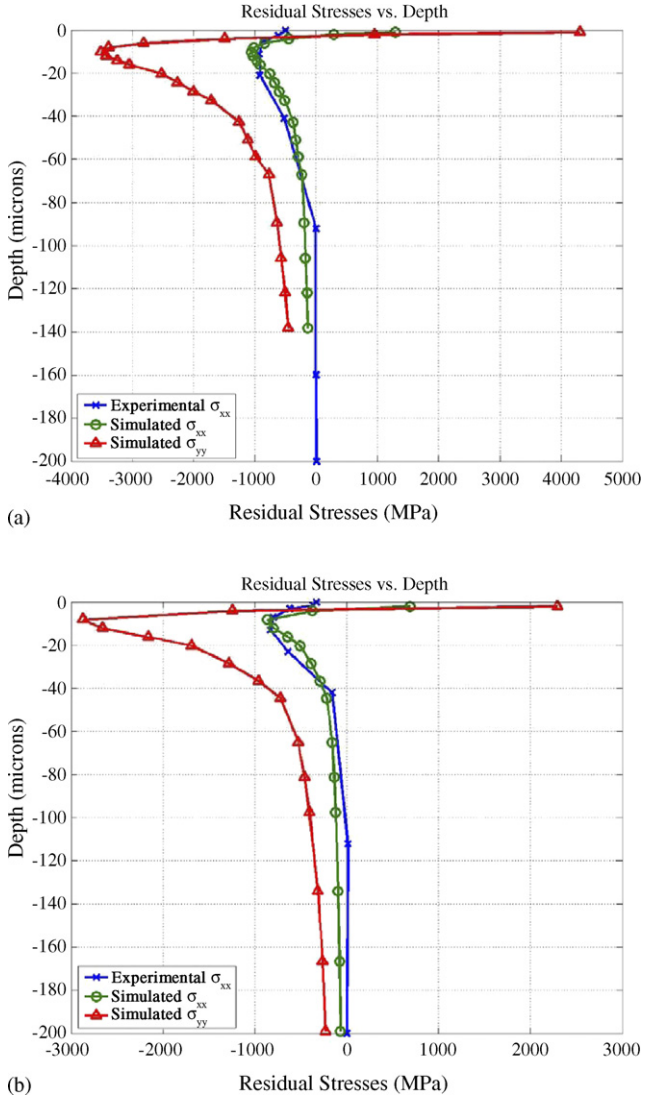


Fig. 6. Comparison of simulations and experimental results of Liu et al. [14] for a nose radius of 0.4 mm: (a) depth of cut of 0.1 mm and (b) depth of cut of 0.2 mm.

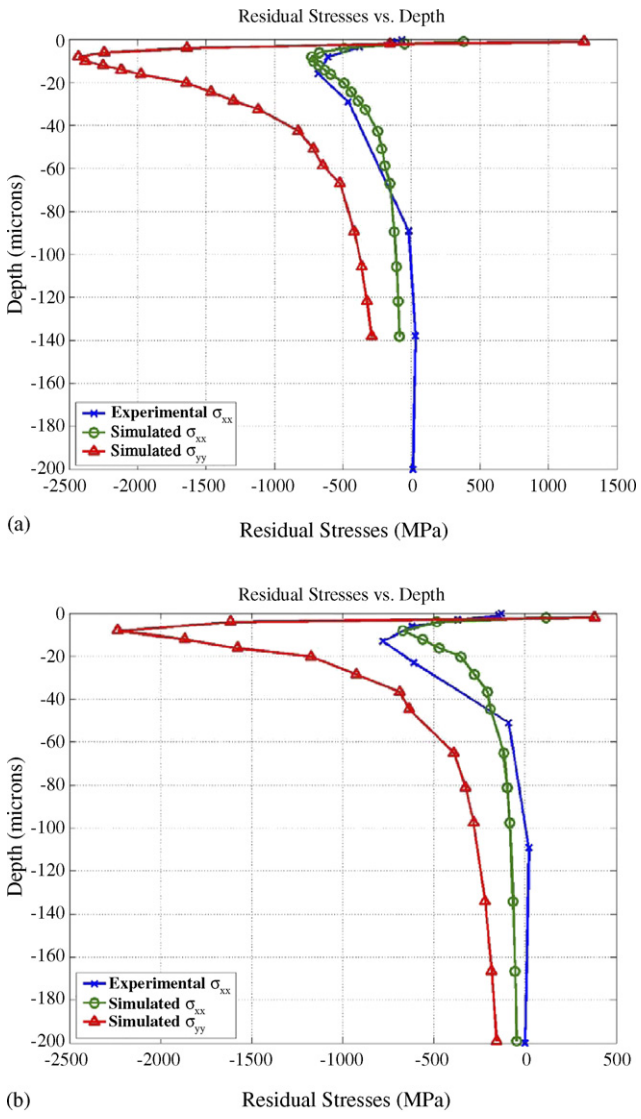


Fig. 7. Comparison of simulated and experimental results of Liu et al. [14] for a nose radius of 0.8 mm: (a) depth of cut of 0.1 mm and (b) depth of cut of 0.2 mm.

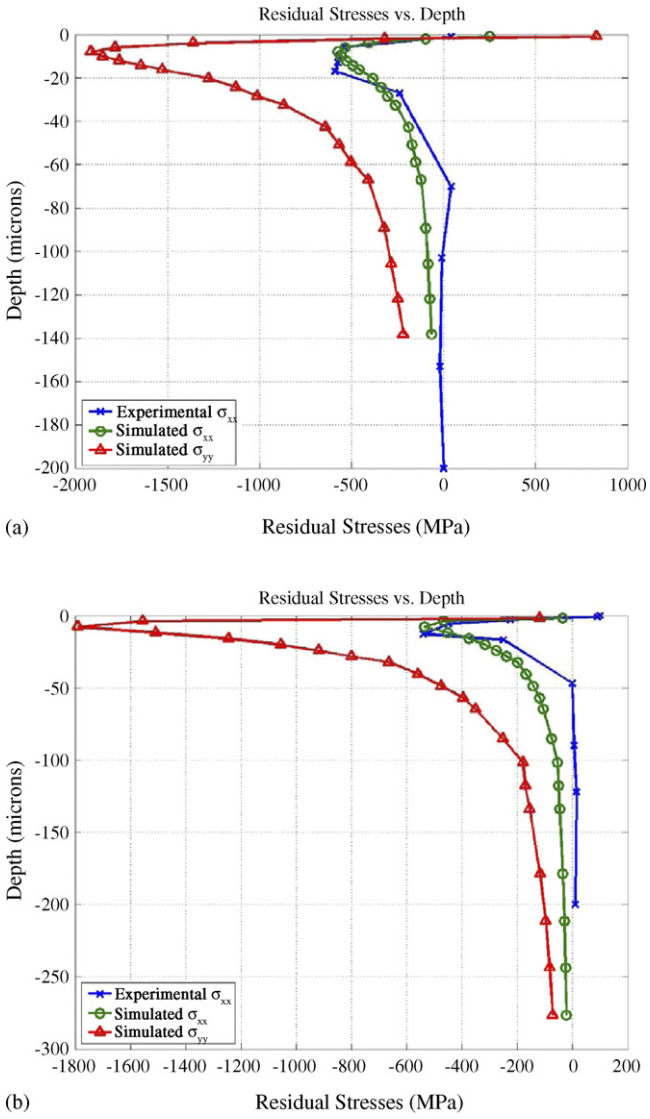


Fig. 8. Comparison of simulated and experimental results of Liu et al. [14] for a nose radius of 1.2 mm: (a) depth of cut of 0.1 mm and (b) depth of cut of 0.2 mm.

X-ray diffraction technique was employed for the measurement of resulting residual stresses along the feed direction as a function of depth from the machined surface.

For the reported experimental conditions, coupled tool, chip and workpiece temperature fields were simulated by using the finite difference method as explained in Section 2. Some of the typical thermal field simulation results for different depths of cut are shown in Figs. 4 and 5. The resulting workpiece thermal fields are then utilized as inputs to the thermo-mechanical model for residual stress predictions. For the fresh tool with a contact span of 50 microns, the simulated residual stresses along the depth from the workpiece surface are shown for various nose radii and depths of cut in Figs. 6–8. It is observed that simulation results and experimental measurements reported in [14] match fairly well. Stresses perpendicular to the feed direction could not be compared due to the lack of experimental data. Some of the observations can be summarized as follows:

(1) In experiments, the maximum value of compressive stresses along the feed direction beneath the surface is observed to decrease with increasing nose radius. Both this trend and magnitude of stresses are matched closely by the simulations.
(2) Experimental measurements are observed to die out at depths closer to the machined surface whereas simulations predict existence of residual stresses at deeper levels. However, the experimentally observed trend of decreasing depths with increasing nose radius is followed closely by simulations.
(3) With increasing depth of cut, tensile residual stresses at the surface predicted by the model decrease consistently for all nose radii. Furthermore, with increasing nose radius, this tensile surface stress is also observed to decrease. For the maximum nose radius of 1.2 mm, stress along the feed direction even becomes compressive if the depth of cut is increased to 0.2 mm. In experiments, on the other hand, the

dependence of the surface stress on the depth of cut is not clear. While it is shifted along the tensile direction for nose radii of 0.4 and 1.2 mm, the shift is in the compressive direction for the nose radius of 0.8 mm. As far as the effect of nose radius is concerned, increasing nose radius leads to a shift in tensile direction as opposed to simulation results.

From these observations it is evident that the shape of stress profile and magnitude of stresses beneath the surface are predicted with better accuracy than at the surface. The difficulty of taking experimental measurements close to the surface might play a role in this mismatch, whereas the deviation becomes less evident when one compares stresses at deeper levels, and hence, important trends can be acquired from these simulations.

## 5. Conclusions

In this paper, residual stresses occurring due to thermo-mechanical effect of machining processes are investigated. A finite-difference-based technique was utilized in the solutions of heat balance equations for determining the thermal fields of the tool, chip and workpiece. Thermal field of workpiece was used in the thermo-mechanical model of the residual stresses. Stresses resulting from thermal and mechanical loading are computed using an analytical elasto-plastic model and a relaxation procedure. The model is verified with experimental data of residual stresses on bearing steel 100Cr6 (JIS SUJ2). Due to its analytical nature the new model allows the prediction of residual stresses quite fast and with acceptable accuracy. Considerable reductions in simulation time, and hence time required for the selection of proper machining conditions are achieved.

## Acknowledgement

The authors acknowledge the Scientific and Technical Research Council of Turkey (TUBITAK) for its support for MISAG-193 Project.

## References

[1] H. Sasahara, The effect on fatigue life of residual stress and surface hardness resulting from different cutting conditions of 0.45%C steel, Int. J. Mach. Tools Manuf. 45 (2005) 131–136.
[2] E.K. Henriksen, Residual stresses in machined surfaces, Trans. ASME 73 (1951) 69–76.
[3] R. M'Saoubi, J.C. Outeiro, B. Changeux, J.L. Lebrun, A.M. Dias, Residual stress analysis in orthogonal machining of standard and resulfurized AISI 316L steels, J. Mater. Process. Technol. 96 (1999) 225–233.
[4] E. Capello, Residual stresses in turning. Part I: influence of process parameters, J. Mater. Process. Technol. 160 (2005) 221–228.
[5] W.B. Saï, N.B. Salah, J.L. Lebrun, Influence of machining by finishing milling on surface characteristics, Int. J. Mach. Tools Manuf. 41 (2001) 443–450.
[6] B.R. Sridhar, G. Devananda, K. Ramachandra, R. Bhat, Effect of machining parameters and heat treatment on the residual stress distribution in titanium alloy IMI-834, J. Mater. Process. Technol. 139 (2003) 628–634.
[7] M.H. El-Axir, A method of modelling residual stress distribution in turning for different materials, Int. J. Mach. Tools Manuf. 42 (2002) 1055–1063.
[8] C.R. Liu, M.M. Barash, Variables governing patterns of mechanical residual stress in a machined surface, J. Eng. Ind. Trans. ASME 104 (1982) 257–264.
[9] J. Rech, A. Moisan, Surface integrity in finish hard turning of case-hardened steels, Int. J. Mach. Tools Manuf. 43 (2003) 543–550.
[10] A.L. Mantle, D.K. Aspinwall, Surface integrity of a high speed milled gamma titanium aluminide, J. Mater. Process. Technol. 118 (2001) 143–150.
[11] C. Genzel, M. Klaus, I. Denks, H.G. Wulz, Residual stress fields in surface-treated silicon carbide for space industry—comparison of biaxial and triaxial analysis using different X-ray methods, Mater. Sci. Eng. A 390 (2005) 376–384.
[12] Y. Quan, B. Ye, The effect of machining on the surface properties of SiC/Al composites, J. Mater. Process. Technol. 138 (2003) 464–467.
[13] D.W. Wu, Y. Matsumoto, The effect of hardness on residual stresses in orthogonal machining of AISI 4340 steel, J. Eng. Ind. Trans. ASME 112 (1990) 245–252.
[14] M. Liu, J. Takagi, A. Tsukuda, Effect of tool nose radius and tool wear on residual stress distribution in hard turning of bearing steel, J. Mater. Process. Technol. 150 (2004) 234–241.
[15] J.D. Thiele, S.N. Melkote, R.A. Peascoe, T.R. Watkins, Effect of cutting-edge geometry and workpiece hardness on surface residual stresses in finish hard turning of AISI 52100 steel, J. Manuf. Sci. Eng. Trans. ASME 122 (2000) 642–649.
[16] R.M. Arunachalam, M.A. Mannan, A.C. Spowage, Surface integrity when machining age hardened Inconel 718 with coated carbide cutting tools, Int. J. Mach. Tools Manuf. 44 (2004) 1481–1491.
[17] R.M. Arunachalam, M.A. Mannan, A.C. Spowage, Residual stress and surface roughness when facing age hardened Inconel 718 with CBN and ceramic cutting tools, Int. J. Mach. Tools Manuf. 44 (2004) 879–887.
[18] J.E. Merwin, K.L. Johnson, An analysis of plastic deformation in rolling contact, Proc. Inst. Mech. Eng. 177 (1963) 676–690.
[19] Y. Jiang, H. Sehitoglu, An analytical approach to elastic–plastic stress analysis of rolling contact, J. Tribol. 116 (1994) 577–587.
[20] K. Jacobus, R.E. DeVor, S.G. Kapoor, Machining-induced residual stress: experimentation and modelling, J. Manuf. Sci. Eng. Trans. ASME 122 (2000) 20–31.
[21] K. Saito, T. Akiyama, T. Kiskinami, Thermal deformation analysis of cutting tools by the finite element method, Bull. Jpn. Soc. Prec. Eng. 7 (1973) 23–36.
[22] T. Akiyama, H. Kakuch, T. Kishinami, Thermal deformation analysis of cutting tools by the finite element method—simulation of thermal deformation, Bull. Jpn. Soc. Prec. Eng. 11 (1977) 139–153.
[23] K. Iwata, K. Osakada, Y. Terasaka, Process modelling of orthogonal cutting by the rigid-plastic finite element method, ASME J. Eng. Mater. Technol. 106 (1984) 132–138.
[24] J.S. Strenkowski, J.T. Carroll III, A finite element model of orthogonal metal cutting, J. Eng. Ind. Trans. ASME 107 (1985) 349–354.
[25] K.C. Ee, O.W. Dillon Jr., I.S. Jawahir, Finite element modelling of residual stresses in machining induced by cutting using a tool with finite edge radius, Int. J. Mech. Sci. 47 (2005) 1611–1628.
[26] S.P. Lo, An analysis of cutting under different rake angles using the finite element method, J. Mater. Process. Technol. 105 (2000) 143–151.
[27] Z.C. Lin, W.L. Lai, H.Y. Lin, C.R. Liu, Residual stresses with different tool flank wear lengths in the ultra-precision machining of Ni–P alloys, J. Mater. Process. Technol. 65 (1997) 116–126.
[28] Z.C. Lin, W.L. Lai, H.Y. Lin, C.R. Liu, The study of ultra-precision machining and residual stress for NiP alloy with different cutting speeds and depth of cut, J. Mater. Process. Technol. 97 (2000) 200–210.
[29] Y.B. Guo, M.E. Barkey, FE-simulation of the effects of machining-induced residual stress profile on rolling contact of hard machined components, Int. J. Mech. Sci. 46 (2004) 371–388.
[30] J. Hua, D. Umbrello, R. Shivpuri, Investigation of cutting conditions and cutting edge preparations for enhanced compressive subsurface residual stress in the hard turning of bearing steel, J. Mater. Process. Technol. 171 (2006) 180–187.
[31] J. Hua, R. Shivpuri, X. Cheng, V. Bedekar, Y. Matsumoto, F. Hashimoto, T.R. Watkins, Effect of feed rate, workpiece hardness and cutting edge on

subsurface residual stress in the hard turning of bearing steel using chamfer + hone cutting edge geometry, Mater. Sci. Eng. A 394 (2005) 238–248.
[32] T.I. El-Wardany, H.A. Kishawy, M.A. Elbestawi, Surface integrity of die material in high speed hard machining, Part 2: microhardness variations and residual stresses, J. Manuf. Sci. Eng. Trans. ASME 122 (2000) 632–641.
[33] M.S. El-Gallab, M.P. Sklad, Machining of aluminium/silicon carbide particulate metal matrix composites. Part IV: residual stresses in the machined workpiece, J. Mater. Process. Technol. 152 (2004) 23–34.
[34] S. Das, M. Klotz, F. Klocke, EDM simulation: finite element-based calculation of deformation, microstructure and residual stresses, J. Mater. Process. Technol. 142 (2003) 434–451.
[35] I. Lazoglu, Y. Altintas, Prediction of tool and chip temperature in continuous and interrupted machining, Int. J. Mach. Tools Manuf. 42 (2002) 1011–1022.
[36] P.L.B. Oxley, Mechanics of Machining: An Analytical Approach to Assessing Machinability, Ellis Horwood Ltd., Chichester, England, 1989.
[37] K.L. Johnson, Contact Mechanics, Cambridge University Press, Cambridge, 1987.
[38] S.P. Timoshenko, J.N. Goodier, Theory of Elasticity, International Edition, McGraw-Hill, Singapore, 1970.
[39] M.T.A. Saif, C.Y. Hui, A.T. Zehnder, Interface shear stresses induced by non-uniform heating of a film on a substrate, Thin Solid Films 224 (1993) 159–167.
[40] J. Lubliner, Plasticity Theory, Macmillan Publishing Company, New York, 1990.